Engineering Geology 323 (2023) 107217

Contents lists available at ScienceDirect

Engineering Geology

journal homepage: www.elsevier.com/locate/enggeo

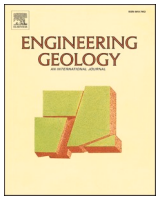

Impact of the compaction behavior of crushed salt on the thermo-hydro-mechanical response of a generic salt repository for heat-generating nuclear waste

Hafssa Tounsi [a], Svetlana Lerche [b], Ralf Wolters [b], Mengsu Hu [a], Jonny Rutqvist [a,*]

[a] Energy Geosciences Division, Lawrence Berkeley National Laboratory, Berkeley, CA 94720, USA
[b] Chair for Geomechanics and Multiphysics Systems, Clausthal University of Technology, Erzstr. 20, D-38678 Clausthal-Zellerfeld, Germany

ARTICLE INFO

Keywords:
Numerical modeling
THM coupling
Rock salt
Crushed salt compaction
Nuclear waste disposal
Safe waste containment

ABSTRACT

Salt formations are a promising host rock for the disposal of heat-emitting nuclear waste due to their ability to heal fractures, high thermal conductivity, and near-zero permeability. This study investigates the concept of waste emplacement in salt formations by placing waste packages in drifts and backfilling them with crushed salt. The aim is to minimize fracturing and restore the initial properties of the host rock.

One of the key issues in assessing the safety and performance of nuclear waste repositories in salt is determining the reconsolidation rate of the crushed salt backfill, which has been traditionally predicted using the C-WIPP model. However, this model was calibrated using data from uniaxial oedometer lab tests, where specimens with high initial porosity values have been compacted to medium porosity values. The observed compaction behavior has then been extrapolated to the low porosity range, leading to a prediction of rapid full reconsolidation of the backfill in less than 20 years. In contrast, the new C-WIPP/TUC model used in this study was calibrated for the medium porosity range, between 17% and 8%, based on more suitable triaxial lab tests. Using coupled Thermo-Hydro-Mechanical (THM) simulations with the TOUGH-FLAC simulator, it was found that the C-WIPP/TUC model predicts a slower reconsolidation rate of the backfill compared to the C-WIPP model, with an average porosity of the backfill remaining roughly 10 times that of natural salt after 10,000 years. The effects of the relatively slow reconsolidation of the crushed salt backfill on the THM behavior of the repository are also examined, highlighting the importance of accurately capturing the behavior of crushed salt for the study of the long-term integrity of a nuclear waste repository in salt.

1. Introduction

Salt formations are one of the most promising host rocks for the disposal of heat-emitting nuclear waste (Hunsche and Hampel, 1999; Hansen and Leigh, 2011; Winterle et al., 2012). The ability of salt to creep promotes the closure and healing of fractures (Chen et al., 2013). Its high thermal conductivity makes it a good candidate to host high heat-emitting radioactive waste (Sweet and McCreight, 1983), and its near-zero permeability makes it a good natural barrier capable of impeding the transport of radionuclides if they are released (Cosenza et al., 1999).

The concept for a geological repository in rock salt that we investigate in this paper is the horizontal emplacement of waste packages in drifts. After the emplacement, the remaining drift openings are backfilled with dry crushed salt in order to re-establish the properties of the host rock and minimize fracturing (Bechthold et al., 2004; Carter et al., 2011). The creep of rock salt induces substantial convergence of the drifts and, consequently, a gradual reconsolidation of the crushed salt backfill (Blanco-Martín et al., 2015a). The healing of rock salt in the excavation damaged zone (EDZ) around the drifts, as well as the compaction of the crushed salt backfill, are expected to restore the initial porosity and permeability of the undisturbed salt formation, ensuring the long-term isolation of radioactive waste packages (Bechthold et al., 2004; Wolters et al., 2012; Blanco-Martín et al., 2015a). Additionally, as compaction takes place, the thermal conductivity and the elastic modulus of the crushed salt increase as well (Bechthold et al., 2004).

The performance of salt as a host rock for the disposal of heat-generating nuclear waste over long timescales has been extensively

* Corresponding author.
E-mail address: jrutqvist@lbl.gov (J. Rutqvist).

https://doi.org/10.1016/j.enggeo.2023.107217
Received 28 February 2023; Received in revised form 3 June 2023; Accepted 15 June 2023
Available online 20 June 2023

investigated. In particular, safety and performance assessments for high-level waste (HLW) disposal in the Gorleben salt dome, in Germany, and in the bedded salt formation of the Waste Isolation Pilot Plant (WIPP) in New Mexico, USA, have contributed to the establishment of a solid basis of knowledge regarding rock salt as a host rock for nuclear waste disposal (Mönig et al., 2013; Kuhlman and Sevougian, 2013). Nevertheless, one of the key issues pertaining to these safety and performance analyses is the determination of the reconsolidation rate of the crushed salt backfill (Kröhn et al., 2012). Over the past years, several tests have been conducted to investigate the behavior of crushed salt compaction (Kröhn et al., 2017; Czaikowski et al., 2020). However, the predominant choice of testing methodology in these investigations was uniaxial oedometer tests, mainly examining the high and medium porosity range (40% to 10%). Lower porosities below 10% were occasionally achieved by increasing temperature and humidity, facilitating compaction (Kröhn et al., 2017). The neglect of high compaction stages with extremely low remaining porosities (less than 5%) can be attributed to several factors (Czaikowski et al., 2020). Firstly, the focus of early experimental studies was not on the long-term contribution of the crushed salt barrier to the safe containment of radioactive waste. Secondly, the description of the compaction behavior at low porosity levels was hindered by the limited precision of experimental devices and methods. Nonetheless, the data derived from these tests have been widely used for the calibration of constitutive models in the literature (Sjaardema and Krieg, 1987; Callahan et al., 1998; Olivella and Gens, 2002; Czaikowski et al., 2020), often extrapolating them to the low porosity range. Besides, these models have been applied to three-dimensional stress states, although the compaction behavior of crushed salt under three-dimensional long-term loading circumstances has not been studied in oedometer testing. Kröhn et al. (2017) reported discrepancies between the results of a triaxial test and an earlier oedometer test, particularly at small porosities. Consequently, previous generic modeling of the long-term behavior of nuclear waste repositories in salt predicted a rapid full reconsolidation of the backfill in less than 20 years (Lerch et al., 2012; Blanco-Martín et al., 2015a; Tounsi et al., 2023).

Moreover, several thermal, hydraulic, mechanical and chemical (THMC) processes take place in a salt repository, mostly as a result of the excavation-induced stress changes and the high temperatures caused by the decay heat of nuclear waste (Blanco-Martín et al., 2016). The reconsolidation rate of the crushed salt backfill would be significantly affected by these THMC processes. Indeed, during the mechanical compaction of granular salt, continuous dynamic microstructural changes occur, including the reorganization of grain aggregates, the creation of microfractures and pressure solution creep (Urai and Spiers, 2017; Hu et al., 2021). Experiments have shown that these microstructural processes are sensitive to moisture, temperature and stress conditions (Spiers et al., 1990; Stormont et al., 2017). Hence, assessing the effect of these THMC processes on the reconsolidation rate is not a simple endeavor.

While it is not possible to measure the long-term (> 10,000 years) evolution of the backfill in situ, a thorough experimental characterization of the crushed salt compaction behavior is required for accurate numerical modeling predictions. A recent collaboration between the United States and Germany (KOMPASS-I) includes the development of experimental procedures for identifying crushed salt behavior in the range of low porosities, with isolated observation of influencing factors on the compaction behavior of crushed salt in long-term triaxial tests, and the enhancement of different existing constitutive models such as the WIPP crushed salt model (C-WIPP), with a particular focus on improving their ability to accurately replicate the porosity and stress-dependent behavior of crushed salt (Czaikowski et al., 2020). Triaxial compression tests were carried out on granular salt specimens with an initial low porosity of about 16% until reaching porosity values of about 8%. The test TUC-V2 (phase 1), which will be explained in detail later on, showed that deviatoric stress has an impact on the compaction rate of the tested specimen, hence invalidating the assumption that viscous compaction is a function of the mean stress only, as is the case in older crushed salt constitutive models such as C-WIPP.

In this paper, the TOUGH-FLAC simulator is used to run coupled THM simulations of a generic salt repository for high-heat-emitting nuclear waste. The objective is to compare the short- and long-term response of the repository, in terms of stress, temperature, saturation, and pore pressure evolution, as well as the integrity of its geological (rock salt) and geotechnical (crushed salt) barriers when using the C-WIPP constitutive model for crushed salt, as opposed to the C-WIPP/TUC (Czaikowski et al., 2020), a new constitutive model for crushed salt developed at Clausthal University of Technology (TUC) to resolve the main limitations of the C-WIPP model.

To achieve this, the TOUGH-FLAC simulation framework is briefly presented, followed by a detailed description of the mechanical, thermal and hydraulic constitutive models used to characterize the behavior of rock salt and crushed salt. The last section presents the results of the comparative THM coupled modeling.

2. TOUGH-FLAC simulator

The TOUGH-FLAC simulator is used in this work. It links TOUGH2 (Pruess et al., 2012), which is an integral finite difference multiphase flow and heat transport simulator, to FLAC3D, which is a finite-difference geomechanical code (Itasca FLAC3D, 2012). The fixed-stress sequential method is used to solve any coupled problem (Kim et al., 2011). In this method, the energy and mass transfer problem is solved first under a constant total stress field. Then, the geomechanical problem is solved using the newly calculated fluid phase pressures, saturations, and temperature fields (Rutqvist et al., 2002).

The thermodynamic state of liquid and gas phases is calculated using the EOS4 module of TOUGH2, which includes vapor pressure lowering effects due to capillary pressure (Pruess et al., 2012).

TOUGH-FLAC has been extended to account for large deformations of the solid by using the updated Lagrangian approach in which the domain grid is updated at each time step (Blanco-Martín et al., 2017). In addition to that, the mechanical simulation allows for updating the flow properties, namely the permeability, the porosity and the capillary pressure, using the newly computed stress/strain fields.

Using the concept of the effective stress and the partitioning of the total strain tensor $\underline{\underline{\varepsilon}}$ into an elastic component $\underline{\underline{\varepsilon}}^{e}$, a viscoplastic component $\underline{\underline{\varepsilon}}^{vp}$ and a thermal component $\underline{\underline{\varepsilon}}^{th}$, the stress-strain constitutive relationship is expressed as follows:

$$\dot{\underline{\underline{\sigma}}}' = \dot{\underline{\underline{\sigma}}} + B\dot{\varpi}\underline{\underline{1}} \quad = \mathbf{H}\left(\dot{\underline{\underline{\varepsilon}}} - \dot{\underline{\underline{\varepsilon}}}^{vp} - A_T\dot{T}\underline{\underline{1}}\right) \tag{1}$$

where $\underline{\underline{\sigma}}'$ is the effective stress tensor, A_T is the drained linear thermal expansion coefficient, T is temperature, B is the Biot coefficient, $\mathbf{H}$ is the drained elasticity tensor and ϖ is the equivalent pore pressure. The latter is defined as the saturation weighted sum of the pressure of the liquid phase p_λ and the pressure of the gaseous phase p_γ plus an interfacial energy term (Coussy, 2004):

$$\varpi = (1 - S_\lambda)p_\gamma + S_\lambda p_\lambda + \int_{S_\lambda}^{1} p_c(S)dS \tag{2}$$

with $p_c = p_\gamma - p_\lambda$ the capillary pressure and S_λ the liquid saturation.

The balance equations solved in TOUGH and FLAC, together with Darcy's law for the filtration velocity vector of fluid phases, Fourier's law for the conductive heat flux and Fick's law for the diffusive velocity vector of water vapor, must be supplemented by the constitutive equations of rock salt (Section 3) and crushed salt (Section 4). All other materials are considered elastic, with constant fluid flow and thermal properties.

The porosity evolution is a function of temperature and pressure of the liquid and gaseous phases via empirical coefficients that depend on

the thermal expansion coefficient, the porosity, the Biot coefficient and the drained bulk modulus K.

$$d\phi = C_p(B,K,\phi)\sum_{\alpha} S_\alpha dp_\alpha + C_T(A_T,\phi)dT + \Delta\phi \tag{3}$$

The term $\Delta\phi$ refers to a porosity correction used to account for volume changes following the geomechanical calculation in FLAC3D in the next time step's resolution of the mass and energy balance equations. Details of the derivation of this term as a function of temperature, phase pressures and total volumetric strain can be found in Kim et al. (2012).

3. Constitutive equations of rock salt

3.1. Mechanical constitutive model: the Lux/Wolters/Lerche model

The Lux/Wolters/Lerche (LWL) model (Lux et al., 2018), an enhanced version of the Lux/Wolters model (Wolters et al., 2012; Blanco-Martín et al., 2016), is used in this paper to describe the mechanical behavior of rock salt.

The viscoplastic strain rate tensor $\dot{\underline{\underline{\varepsilon}}}^{\mathrm{vp}}$ in the LWL model is partitioned into viscous shear strain rate $\dot{\underline{\underline{\varepsilon}}}^{\mathrm{vs}}$, damage-induced strain rate $\dot{\underline{\underline{\varepsilon}}}^{\mathrm{d}}$ resulting from shear or tensile failure and healing-induced strain rate $\dot{\underline{\underline{\varepsilon}}}^{\mathrm{h}}$:

$$\dot{\underline{\underline{\varepsilon}}}^{\mathrm{vp}} = \dot{\underline{\underline{\varepsilon}}}^{\mathrm{vs}} + \dot{\underline{\underline{\varepsilon}}}^{\mathrm{d}} + \dot{\underline{\underline{\varepsilon}}}^{\mathrm{h}} \tag{4}$$

The viscous component is based on the constitutive model mod-Lubby2 (Lerche, 2012). It is purely deviatoric and takes into account transient and steady-state creep mechanisms, as follows:

$$\dot{\underline{\underline{\varepsilon}}}^{\mathrm{vs}} = \frac{3}{2}\dot{\varepsilon}^{\mathrm{vs}}_{\mathrm{vM}}\,\underline{\underline{J}};\quad \underline{\underline{J}} = \underline{\underline{\sigma}}^{\mathrm{d}}/\sigma_{\mathrm{vM}};\quad \dot{\varepsilon}^{\mathrm{vs}}_{\mathrm{vM}} = \dot{\varepsilon}^{\mathrm{tr}}_{\mathrm{vM}} + \dot{\varepsilon}^{\mathrm{ss}}_{\mathrm{vM}} \tag{5}$$

where $\underline{\underline{\sigma}}^{\mathrm{d}} = \underline{\underline{\sigma}} - \frac{1}{3}\mathrm{tr}\left(\underline{\underline{\sigma}}\right)\,\underline{\underline{1}}$ is the deviatoric stress tensor and $\sigma_{\mathrm{vM}} = \sqrt{\frac{3}{2}\,\underline{\underline{\sigma}}^{\mathrm{d}} : \underline{\underline{\sigma}}^{\mathrm{d}}}$ is the von Mises equivalent stress. The subscript vM is used to designate equivalent von Mises strain terms as well.

The two equivalent viscous strain-rate components are expressed as follows:

$$\dot{\varepsilon}^{\mathrm{tr}}_{\mathrm{vM}} = \frac{1}{\overline{\eta}_{\mathrm{k}}(\sigma_{\mathrm{vM}})}\left\langle 1 - \frac{\varepsilon^{\mathrm{tr}}_{\mathrm{vM}}}{max\ \varepsilon^{\mathrm{tr}}_{\mathrm{vM}}}\right\rangle \sigma_{\mathrm{vM}} \tag{6}$$

$$\dot{\varepsilon}^{\mathrm{ss}}_{\mathrm{vM}} = \frac{1}{\overline{\eta}_{\mathrm{m}}(\sigma_{\mathrm{vM}}T)}\sigma_{\mathrm{vM}} \tag{7}$$

The Maxwell and Kelvin viscosity moduli, $\overline{\eta}_{\mathrm{m}}$ and $\overline{\eta}_{\mathrm{k}}$, are expressed as follows:

$$\overline{\eta}_{\mathrm{k}}(\sigma_{\mathrm{vM}}) = \overline{\eta}^{*}_{\mathrm{k}}\ exp(k_2\sigma_{\mathrm{vM}}) \tag{8}$$

$$\overline{\eta}_{\mathrm{m}}(\sigma_{\mathrm{vM}},T) = \overline{\eta}^{**}_{\mathrm{m}}\left(\frac{\sigma_{\mathrm{vM}}}{\sigma_{\mathrm{r}}}\right)^{a} exp(m\sigma_{\mathrm{vM}})\ exp(lT) \tag{9}$$

The Macauley Brackets $\langle\cdot\rangle$ are used because the transient creep saturates at the maximum equivalent Kelvin strain, determined as follows:

$$max\ \varepsilon^{\mathrm{tr}}_{\mathrm{vM}} = \frac{\sigma_{\mathrm{vM}}}{\overline{G}_{\mathrm{k}}(\sigma_{\mathrm{vM}})} \tag{10}$$

with $\overline{G}_k$ the Kelvin shear modulus, expressed as follows:

$$\overline{G}_{\mathrm{k}}(\sigma_{\mathrm{vM}}) = \overline{G}^{*}_{\mathrm{k}}\left(\frac{\sigma_{\mathrm{vM}}}{\sigma_{\mathrm{r}}}\right)^{b} exp(k_1\sigma_{\mathrm{vM}}) \tag{11}$$

where $\overline{\eta}^{*}_{\mathrm{k}}$, $\overline{\eta}^{**}_{\mathrm{m}}$, $\overline{G}^{*}_{\mathrm{k}}$, m, l, a, b, k_1 and k_2 are material parameters. σ_{r} is a reference stress set equal to 1 MPa.

The expression of the damage strain rate component $\dot{\underline{\underline{\varepsilon}}}^{\mathrm{d}}$ and the dependencies of elastic parameters on damage can be found in Lux et al. (2018). The expression of the healing component $\dot{\underline{\underline{\varepsilon}}}^{\mathrm{h}}$ is presented in detail in Lerche (2012) and Wolters (2014). In total, 40 parameters were used to describe all the stages of deformation: elasticity, transient and stationary creep, shear and tensile damage and healing. All of these parameters, except for parameters a and b for creep behavior in the area of low deviatoric stresses ($\sigma_{\mathrm{vM}} < 5$ MPa), were obtained from TUC laboratory database (Lerche, 2012; Lux et al., 2018).

3.2. Hydraulic and thermal constitutive models

Thermomechanically-induced damage results in the creation of micro-fissures, which can lead to the generation of a secondary permeability when viscoplastic volumetric strain $\varepsilon^{\mathrm{vp}}_{\mathrm{v}}$ exceeds a dilatancy threshold $\varepsilon^{\mathrm{vp}}_{\mathrm{v},0}$ and damage-induced micro-fissures begin to coalesce (Wolters et al., 2012). This permeability-dilatancy relationship is expressed as follows:

$$\begin{cases} log(k) = log(k_0) + \left\langle log\left(\varepsilon^{\mathrm{vp}}_{\mathrm{v}}\right) - log\left(\varepsilon^{\mathrm{vp}}_{\mathrm{v},0}\right) + \dfrac{r}{ln(10)}exp\left(s\sigma'_{\perp 2}\right)\left(\mathrm{Ei}\left(t\varepsilon^{\mathrm{vp}}_{\mathrm{v}}\right) - \mathrm{Ei}\left(t\varepsilon^{\mathrm{vp}}_{\mathrm{v},0}\right)\right)\right\rangle ; \varepsilon^{\mathrm{vp}}_{\mathrm{v}} \geqslant \varepsilon^{\mathrm{vp}}_{\mathrm{v},0} \\ k = k_0 ; \varepsilon^{\mathrm{vp}}_{\mathrm{v}} < \varepsilon^{\mathrm{vp}}_{\mathrm{v},0} \end{cases} . \tag{12}$$

where k_0 is the initial/minimum salt rock permeability, $\sigma'_{\perp 2}$ is the effective stress perpendicular to the orientation of the micro-fissures, $\mathrm{Ei}(x)$ is the exponential integral function, and r, s and t are material constants.

Intrinsic permeability can also increase as a result of hydraulically-induced damage, which occurs when the fluid pressure ϖ exceeds the minimum (i.e., least compressive) principal stress σ_3, causing the grain boundaries to open and fluid to infiltrate (Wolters et al., 2012):

$$log(k) = i_1 + i_2 arctan\left(i_3\Delta P_{\mathrm{fl}}\right) + i_4 exp\left(i_5\Delta P_{\mathrm{fl}}\right)\ ,\quad \Delta P_{\mathrm{fl}} > 0 \tag{13}$$

where $\Delta P_{\mathrm{fl}} = \varpi + \sigma_3$ and i_1, i_2, i_3, i_4 and i_5 are material parameters.

The Biot coefficient of undisturbed rock salt, initially very low, is assumed to increase with rock salt damage level using the following analytical formula (Hou, 2002; Kansy, 2007):

$$B = max\left(\frac{D}{0.1},\ 1 - exp\left(\frac{\sigma_{\mathrm{vM}}mD}{0.1 - D}\right)\right) \tag{14}$$

where D is the damage variable and m is the LWL model parameter controlling the equivalent stress's influence on the Maxwell viscosity coefficient (see Eq. 9).

Nevertheless, healing of rock salt can help restore the undisturbed values of intrinsic permeability and Biot's coefficient.

The changes in permeability and porosity affect the magnitude of capillary pressure. To take account of this, the capillary pressure is scaled using the following formula (Leverett, 1941):

$$p_{\mathrm{c}} = p_{\mathrm{c}_0}\left(\frac{k_0/\phi_0}{k/\phi}\right)^{le} \tag{15}$$

ϕ_0 is the initial porosity of the porous medium and p_{c_0} is the unscaled capillary pressure, expressed using the van Genuchten (VG) model:

$$p_{c_0} = -P_0\left([S^*]^{-1/\mu} - 1\right)^{1-\mu} \;;\; p_{c0} \geq P_{\max} \tag{16}$$

where $S^* = (S_\lambda - S_{\lambda r})/(1 - S_{\lambda r})$, S_λ is the liquid saturation and parameters P_0, μ, $S_{\lambda r}$, $P_{\max}$ and le are material constants.

Corey's curves are used to express liquid and gas relative permeabilities.

Regarding the thermal parameters, the evolution of thermal conductivity and heat capacity of rock salt with temperature is described using the following empirical expressions derived within the BAMBUS project (Bechthold et al., 2004):

$$\begin{cases} C_p = 855 + 0.1777\,T \\ \lambda_{\text{salt}} = 5.734 - 1.838 \times 10^{-2}T + 2.86 \times 10^{-5}T^2 - 1.51 \times 10^{-8}T^3 \end{cases} \tag{17}$$

4. Constitutive equations of crushed salt

4.1. Mechanical constitutive models: the C-WIPP and the C-WIPP/TUC models

We compare in this section two constitutive models: a modified version of the C-WIPP model implemented by ITASCA in FLAC3D (Sjaardema and Krieg, 1987; Itasca FLAC3D, 2012; Blanco-Martín et al., 2016) and C-WIPP/TUC (Czaikowski et al., 2020).

The elastic strain tensor $\underline{\underline{\varepsilon}}^{\,e}$ is non-linear in both models and is related to the effective stress tensor $\underline{\underline{\sigma}}'$ by Hooke's law as follows:

$$\dot{\underline{\underline{\sigma}}}' = 2G\left(\dot{\underline{\underline{\varepsilon}}}^{\,e} - \frac{1}{3}\mathrm{tr}\left(\dot{\underline{\underline{\varepsilon}}}^{\,e}\right)\,\underline{\underline{1}}\right) + K\mathrm{tr}\left(\dot{\underline{\underline{\varepsilon}}}^{\,e}\right)\,\underline{\underline{1}} \tag{18}$$

The drained bulk modulus K and the shear modulus G are assumed to increase, exponentially, with crushed salt density ρ during compaction. When ρ becomes equal to the drained density of rock salt ρ_{salt}, K and G take the values of the elastic parameters of undisturbed rock salt K_{salt} and G_{salt}, respectively.

$$\begin{cases} K = K_{\text{salt}}\,\exp(K_1(\rho - \rho_{\text{salt}})) \\ G = G_{\text{salt}}\,\exp(G_1(\rho - \rho_{\text{salt}})) \end{cases}. \tag{19}$$

Knowing the initial values of the density and the elastic moduli of crushed salt, the parameters K_1 and G_1 can be determined.

Both models agree on the partition of the viscoplastic strain rate tensor $\dot{\underline{\underline{\varepsilon}}}^{\,vp}$ into a viscous compaction component $\dot{\underline{\underline{\varepsilon}}}^{\,vc}$ and a viscous shear component $\dot{\underline{\underline{\varepsilon}}}^{\,vs}$:

$$\dot{\underline{\underline{\varepsilon}}}^{\,vp} = \dot{\underline{\underline{\varepsilon}}}^{\,vc} + \dot{\underline{\underline{\varepsilon}}}^{\,vs} \tag{20}$$

The compaction strain rate component is only active if the mean effective stress $\sigma'_m = \frac{1}{3}\mathrm{tr}\left(\underline{\underline{\sigma}}'\right)$ is compressive. It is expressed as follows in both models:

$$\dot{\underline{\underline{\varepsilon}}}^{\,vc} = \dot{\varepsilon}^{vc}\left(\frac{1}{3}\,\underline{\underline{1}} - \beta\,\underline{\underline{J}}\right) \tag{21}$$

The volumetric compaction strain rate $\dot{\varepsilon}^{vc}$ and the parameter β are not expressed in the same way in the C-WIPP and C-WIPP/TUC models.

The viscous shear component is purely deviatoric and takes into account transient and steady-state creep mechanisms (see eq. 5) which are expressed differently in the C-WIPP and the C-WIPP/TUC models.

4.1.1. The modified C-WIPP model

The viscous compaction strain rate in the C-WIPP model is a function of density and the mean effective stress only, as follows:

$$\dot{\varepsilon}^{vc} = \frac{B_0}{\rho}\left[1 - exp\left(-B_1\sigma'_m\right)\right]exp(B_2\rho) \tag{22}$$

where B_0, B_1 and B_2 are constant material parameters. When density becomes equal to rock salt density, $\dot{\varepsilon}^{vc}$ is set to zero.

It should be noted that the viscous compaction strain rate in the original C-WIPP model (Itasca FLAC3D, 2012) is irreversible, which means that density is not allowed to decrease. This issue has been resolved in the modified version in which density can increase and decrease depending on the volumetric strain's evolution (Blanco-Martín et al., 2016).

The parameter β in Eq. 21 is a constant, set equal to one. This allows to cancel lateral compaction strain rate components for a uniaxial compression scenario but results in a discontinuous formulation of the uniaxial-isotropic loading transition.

The transient creep component is expressed exactly as in the WIPP model. It is proportional to the steady-state component $\dot{\varepsilon}^{ss}_{vM}$ as follows:

$$\dot{\varepsilon}^{tr}_{vM} = H\dot{\varepsilon}^{ss}_{vM}, H = \begin{cases} B_3 - B_4\varepsilon^{tr}_{vM}, \dot{\varepsilon}^{ss}_{vM} \geq \dot{\varepsilon}^{ss*}_{vM} \\ B_3 - B_4\left(\dfrac{\dot{\varepsilon}^{ss*}_{vM}}{\dot{\varepsilon}^{ss}_{vM}}\right)\varepsilon^{tr}_{vM}, \dot{\varepsilon}^{ss}_{vM} < \dot{\varepsilon}^{ss*}_{vM} \end{cases} \tag{23}$$

where B_3, B_4 and $\dot{\varepsilon}^{ss*}_{vM}$ are material constants.

The steady-state flow component $\dot{\varepsilon}_{ss}$ is equal to a Norton-type power law in which the equivalent von Mises stress is divided by the ratio between the current density and the rock salt, density as shown below:

$$\dot{\varepsilon}^{ss}_{vM} = A_1\left(\frac{\rho_{\text{salt}}}{\rho}\frac{\sigma_{vM}}{\sigma_r}\right)^n exp\left(-\frac{A_2}{T}\right) \tag{24}$$

where σ_r is a reference stress ($\sigma_r = 1$ MPa) and A_1, A_2 and n are material constants. A_2 is widely assumed to be equal to Q/R, where R is the universal gas constant and Q is the activation energy.

4.1.2. The C-WIPP/TUC model

The viscous compaction strain rate in the C-WIPP/TUC model is formulated in terms of porosity instead of density. The dependency between the volume compaction of crushed salt and porosity is described using a more flexible mathematical formulation compared to C-WIPP model, allowing it to fit different experimental data. Moreover, in accordance with the outcome of recent triaxial tests on crushed salt (see phase 1 (first 150 days) of the test TUC-V2 presented in Section 4.1.4), the C-WIPP/TUC model takes into account the effect of the deviatoric stress component on the compaction behavior, as follows:

$$\dot{\varepsilon}^{vc} = C_0\left[1 - exp\left(-C_{1m}\sigma'_m + C_{1v}\sigma_{vM}\right)\right]\frac{exp(C_{2e}\phi)}{1-\phi}\left(\frac{\phi}{C_3}\right)^{C_{2p}} \tag{25}$$

where C_0, C_{1m}, C_{1v}, C_{2e}, C_{2p} and C_3 are constant material parameters. It can be seen in Eq. 25 that for a fully compacted crushed salt, i.e., $\phi = 0$, the model C-WIPP/TUC ensures that the viscous compaction strain rate will be equal to zero.

The parameter β is a variable in the C-WIPP/TUC model. It depends on α the angle between the direction of isotropic stress and the direction of deviatoric stress, allowing a continuous transition between isotropic and triaxial loading conditions as follows:

$$\beta = \beta_1(tan(\alpha))^{\beta_2} \;;\; tan(\alpha) = \frac{1}{3}\frac{\sigma_{vM}}{\sigma'_m} \tag{26}$$

with β_1 and β_2 material parameters.

The viscous component of the C-WIPP/TUC model as presented in Czaikowski et al. (2020) is based on the WIPP model. In this paper, the modLubby2 model (Lerche, 2012) described in the previous section is used instead. The transient term has been kept exactly the same, whereas the steady-state component has been enriched by accounting for the effect of porosity on the Maxwell viscosity modulus $\overline{\eta}_m(\sigma_{vM}, T, \phi)$, in accordance with new experimental results suggesting that creep is faster for high porosities. The new expression of the Maxwell viscosity modulus is the following:

$$\overline{\eta}_{\mathrm{m}}(\sigma_{\mathrm{vM}}, T, \phi) = \overline{\eta}_{\mathrm{m}}^{**}\left(\frac{\sigma_{\mathrm{vM}}}{\sigma_{\mathrm{r}}}\right)^{a} exp(m\sigma_{\mathrm{vM}})\, exp(lT)\left(1-\frac{\phi}{\phi_0+\delta}\right)^{c} \quad (27)$$

where c and δ are additional material parameters.

It should be noted that, contrary to the WIPP model, the modLubby2 model captures the low-deviatoric stress creep regime and has been calibrated against creep data at high stress levels and medium stress levels (using lab test data), as well as at low-stress levels (using in situ measurement data). Hence, its steady-state strain rate and transient strain limit predictions at low deviatoric stress are orders of magnitude higher than WIPP model predictions.

In addition to that, using the modLubby2 model to characterize crushed salt creep allows for a unified formulation with the LWL model used for rock salt and a smoother transition from granular salt to rock salt in the numerical simulations.

Moreover, in zones with a tensile stress state, the C-WIPP/TUC model predicts a porosity increase, and the tensile stress is cut off at zero effective stress. The resulting strain rates in the direction of tensile stresses are calculated using Hooke's law and set to zero otherwise. This tension-cut-off-induced deformation is of high importance for handling zones where porosity increases due to the settling of crushed salt.

4.1.3. Material parameters

Table 1 lists the values of the material parameters of the C-WIPP and C-WIPP/TUC models, including the initial calibrated values of the bulk and shear moduli.

The values of the C-WIPP model parameters have traditionally been used in the literature to characterize the creep of crushed salt (DBE, 2001; Itasca FLAC3D, 2012; Blanco-Martín et al., 2015a). These parameters, as previously stated, have only been calibrated against oedometric tests on granular salt samples with a high initial porosity.

The parameters of the C-WIPP/TUC model were determined based on recent multi-stage tests with isotropic and deviatoric load stages on pre-compacted specimens with a low initial porosity of about 16% (Czaikowski et al., 2020).

4.1.4. Model comparison against laboratory tests

Two triaxial long-term tests were chosen to show the similarities and the differences between the two model versions C-WIPP and C-WIPP/TUC and to distinguish the advantages of the C-WIPP/TUC model. The detailed description of these tests can be found in the final report of KOMPASS-I project (Czaikowski et al., 2020); the analysis of the information, that can be derived from these tests for the development or for the validation of a constitutive model, can be found in Düsterloh et al. (2022b).

Table 1
Material parameters of the C-WIPP and C-WIPP/TUC models.

C-WIPP	C-WIPP/TUC
K [MPa] 150	K [MPa] 375
G [MPa] 70	G [MPa] 263
B_0 [kg m^{-3} s^{-1}] 8.6×10^{8}	$\overline{\eta}_{\mathrm{m}}^{**}$ [MPa s] 1.75×10^{19}
B_1 [MPa^{-1}] 0.195	m [MPa^{-1}] −0.18
B_2 [m^3 kg^{-1}] -1.72×10^{-2}	l [K^{-1}] −0.05
B_3 [−] 4.56	$\overline{G}_{\mathrm{k}}^{*}$ [MPa] 3.64×10^{5}
B_4 [−] 127	$\overline{\eta}_{\mathrm{k}}^{*}$ [MPa s] 4.15×10^{9}
$\dot{\varepsilon}_{\mathrm{eq}}^{\mathrm{ss}*}$ [s^{-1}] 5.39×10^{-8}	k_1 [MPa^{-1}] −0.13
n [−] 4.9	k_2 [MPa^{-1}] −0.12
A_1 [s^{-1}] 1.45×10^{-6}	c [−] 8
A_2 [K] 6038	δ [−] 0.01
	C_0 [s^{-1}] 1.84896×10^{-17}
	$C_{1\mathrm{m}}$ [MPa^{-1}] 0.66
	$C_{1\mathrm{v}}$ [MPa^{-1}] 0.25
	$C_{2\mathrm{e}}$ [−] 151.9
	$C_{2\mathrm{p}}$ [−] 0.2
	C_3 [−] 0.165
	β_1 [−] 3.6
	β_2 [−] 1

1. The triaxial test TK-31, shown in Fig. 1a, was conducted by the German Federal Institute for Geosciences and Natural Resources BGR (Bundesanstalt für Geowissenschaften und Rohstoffe). It involves 5 isotropic load stages and allows to validate the dependencies from the porosity and from the mean stress for the test duration of 300 days and for the following ranges of the influencing factors: the porosity ϕ between 16.5% and 6.8%, and the mean stress σ_{m} between 10 MPa and 20 MPa. In Fig. 1b, the results of the back-analysis for test TK-31 demonstrate an excellent agreement between the measured volumetric strain rate evolution and the calculated one using the C-WIPP/TUC model. However, as can be seen in Fig. 2a, we can achieve a similar level of quality in the back-analysis of volumetric strains using the C-WIPP model. The difference in the quality of the back-analysis becomes apparent when examining individual strain components, as demonstrated in Fig. 2b. While the C-WIPP model is obviously unable to correctly reproduce the distribution of strains for nearly triaxial load states, the C-WIPP/TUC model matches the measurement results considerably better.
2. The triaxial test TUC-V2 (phase 1) conducted by TUC involves 5 isotropic load stages as well as 5 intermediate deviatoric load stages to isolate the influence of the deviatoric load on the compaction behavior of the crushed salt (see Fig. 3a). The test allows to validate the dependencies of the compaction behavior on porosity, on mean stress level and on the deviatoric stresses for the test duration of 150 days (only test phase 1 of 5 test phases till the end of the test) and for the following ranges of the influencing factors: the porosity ϕ between 16.7% and 9.3%, the mean stress σ_{m} between 4 MPa and 20 MPa, and a deviatoric stress of 8 MPa in several load stages of the test phase 1. The difference in the results of the back-analysis of the deviatoric phases of test TUC-V2 with the models C-WIPP and C-WIPP/TUC can be clearly seen in Fig. 3b. The C-WIPP model does not react at all to the changing deviatoric stress, because this influencing factor is not considered in the model. Meanwhile, the C-WIPP/TUC model responds qualitatively and quantitatively according to the jumps in the measured values of the volumetric strain rate in these deviatoric phases.

4.2. Hydraulic and thermal constitutive models

To account for the decrease of permeability that occurs during crushed salt compaction, the following empirical expression is utilized (Bechthold et al., 2004):

$$k_{\mathrm{cr}} = 5.68 \times 10^{-11}\phi^{4.36} \quad (28)$$

Nevertheless, crushed salt permeability can increase again if hydraulically induced damage takes place. In that case, Eq. 13 will be used.

The Biot coefficient of crushed salt is expressed as $1 - K/K_s$, with K_s being the bulk modulus of solid grains.

Van Genuchten model and Corey's curves are used to express capillary pressure and liquid and gas relative permeabilities, respectively. Similarly with rock salt, capillary pressure in crushed salt is scaled when porosity and permeability change using Eq. 15.

Crushed salt's thermal conductivity increases as crushed salt is compacting. To account for it, the following empirical expression is used (Bechthold et al., 2004):

$$\lambda_{\mathrm{cr}} = -270\phi^4 + 370\phi^3 - 136\phi^2 + 1.5\phi + 5 \quad (29)$$

Crushed salt has a temperature-dependent heat capacity that is expressed in the same way as rock salt.

Finally, note that when the porosity of crushed salt reaches the porosity of natural salt, empirical equations for natural salt are used instead.

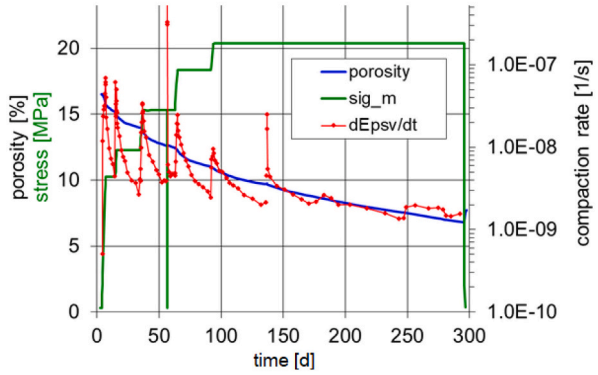

(a) Load history and measured porosity evolution.

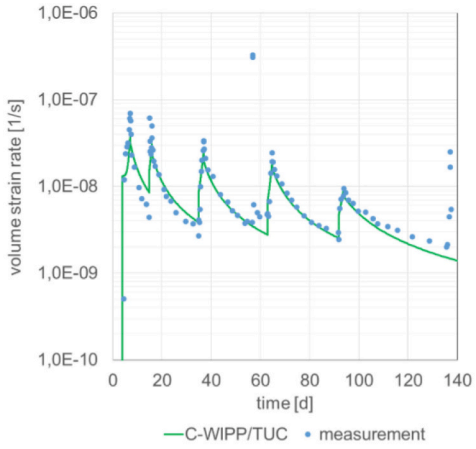

(b) Measured and calculated volumetric strain rate evolution

Fig. 1. Long-term compaction test TK-31 conducted by BGR (Czaikowski et al., 2020) and the result of the back-analysis of the measured volumetric strain rate evolution using the C-WIPP/TUC model.

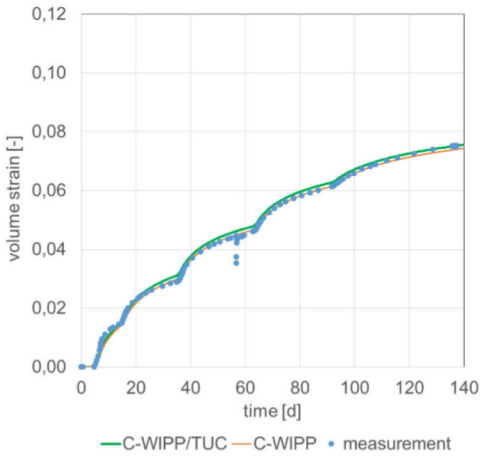

(a) volumetric strain

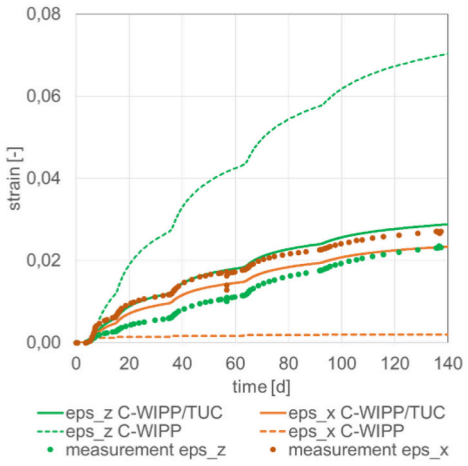

(b) Vertical and horizontal stresses

Fig. 2. Comparison of the results of the back-analysis of test TK-31 with the models C-WIPP and C-WIPP/TUC.

5. Numerical modeling of a generic repository

5.1. Model geometry

The TOUGH-FLAC model geometry of the generic salt repository is shown in Fig. 4. It has been previously used by Blanco-Martín et al. (2015b) to simulate a generic salt repository for conventional canisters, containing 10 Pressurized Water Reactor (PWR) elements and stored intermittently out of the reactor for a relatively short period of 20 years. This geometry has been built by considering a repetitive symmetry due to parallel and evenly spaced horizontal emplacement drifts and waste packages along them. Hence, the model extends horizontally to the mid-distance between two emplacement tunnels, which is 25 m. The out-of-plane width is equal to 1 m. Vertically, the repository is located in the middle of a 400-m-thick salt layer, at a depth of 600 m below the ground surface. Two 400-m-thick sandstone layers confine the rock salt. The drifts are 4.5 m wide and 3.5 m high and the cylindrical waste canisters emplaced inside of them have a diameter of 1.6 m.

5.2. Initial and boundary conditions

A geothermal gradient of 0.03°C/m is initially applied to the model, with the ground surface temperature equal to 10 °C. This corresponds to a temperature of 28 °C at the repository level. The stress state is initially isotropic, equal to the lithostatic stress, and the water pressure is hydrostatic, with the water table located at ground level.

As to the mechanical boundary conditions, strains in the out-of-plane direction are assumed to be zero. The displacement normal to the lateral and bottom boundaries is constrained. A no-flow (heat and fluid) boundary condition is assigned to the lateral boundaries as well as along the inner boundary of the waste canister. At the top and bottom boundaries, temperature and liquid pressure are maintained at their initial values.

5.3. Simulation phases and material parameters

The simulation starts with the excavation of the drift at a constant temperature. During this phase, the stresses within the drift and the waste canister elements are set to zero and the pressure is set to the

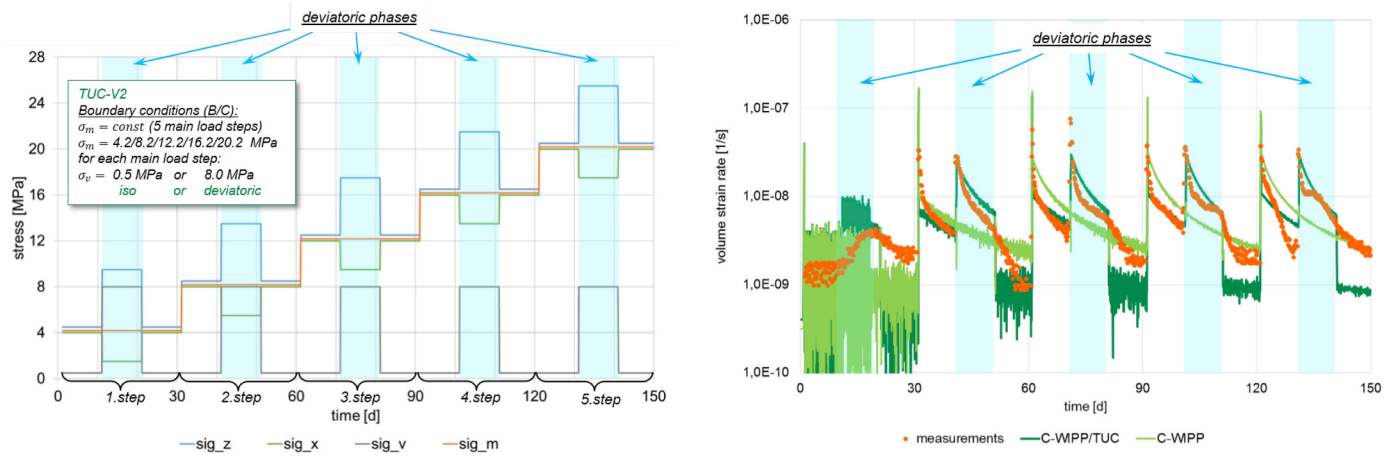

(a) Load history (b) volumetric strain rate

Fig. 3. Comparison of the results of the back-analysis of test TUC-V2 (phase 1) with the models C-WIPP and C-WIPP/TUC.

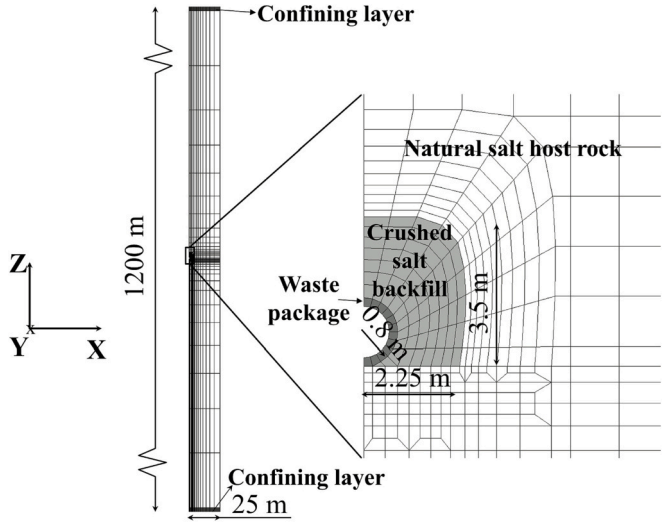

Fig. 4. Two-dimensional model geometry of the salt repository (Blanco-Martín et al., 2015b).

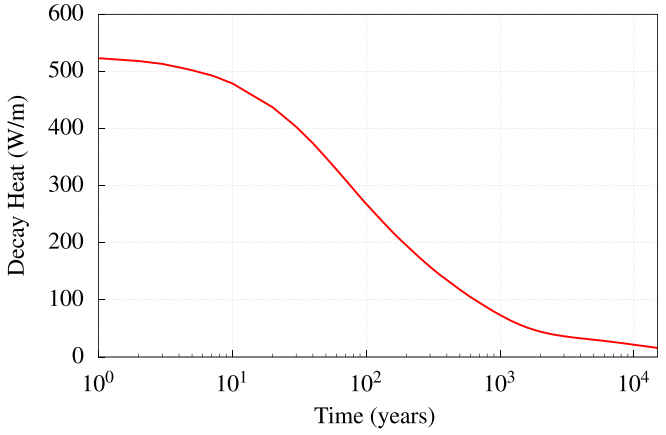

Fig. 5. Heat power per meter drift for a 37-PWR canister after 100 years of interim storage (canister spacing is 20 m).

atmospheric pressure. The resulting pore pressure and stress distributions serve as an initial state for the subsequent post-closure phase. The post-closure phase begins with the instantaneous emplacement of the cylindrical waste canister and the drift backfilling with dry crushed salt. This is done by assigning steel properties to the waste package elements. The drift elements are assigned a constitutive model for crushed salt. The stress state in these elements is initialized using the densities of crushed salt and the steel canister, and a FLAC3D simulation is performed in order to start the TOUGH-FLAC simulation from a state of mechanical equilibrium. Next, the time is reset to zero. The temperature in the drift and canister elements remains unchanged from before the excavation and the pore pressure is set to atmospheric pressure. An initial gas saturation of 0.985 is assigned to the crushed salt backfill elements, while the canister elements are considered saturated with gas. The heat load function (i.e., total heat power per meter drift), shown in Fig. 5 is applied to the waste package. This function is applicable to a large disposal canister that contains 37-PWR fuel elements, removed from a nuclear reactor and disposed of 100 years later (Rutqvist, 2020). Note that this function is scaled for a center-to-center spacing of 20 m between waste canisters.

Table 2 lists the THM properties of rock salt, crushed salt and

Table 2
THM properties of rock salt, crushed salt and sandstone confining layers.

Parameter	Rock salt	Crushed salt	Sandstone
Bulk density [kg/m^3]	2200*	1650	2600*
Porosity [−]	0.002	0.25	0.12
Bulk modulus [GPa]	18.116	Table 1	37.879*
Shear modulus [GPa]	9.843	Table 1	19.531*
Grain Specific heat [J/kg °C]	860	860	900*
Thermal conductivity [W/m °C]	4	1.6	1.8*
Thermal expansion coefficient* × 10^{-5} [°C $^{-1}$]	4	4	1
Diffusion coefficient for water vapor* (m^2/s)	2.13 × 10^{-5}	2.13 × 10^{-5}	2.13 × 10^{-5}
Bulk Permeability [m^2]	10^{-22}	1.35 × 10^{-13}	10^{-17}*
Biot coefficient [−]	0.003	1	1*
Relative Permeability Parameters (Corey's curves /VG)			
Residual liquid saturation * [−]	0.1	0.1	0.02 (VG)
Residual gas saturation * [−]	0	0	0.01 (VG)
Capillary pressure parameters (VG)			
μ* [−]	0.6	0.6	0.6
P_0 [MPa]	5.7	4 × 10^{-4}	3.6
$S_{\lambda r}$* [−]	0.01	0.01	0.01
Leverett parameter *le** [−]	0.57	0.57	–

* Constant values.

sandstone layers. Many of these values come from prior research on natural and granular salt (Bechthold et al., 2004; Olivella et al., 2011; Camphouse et al., 2012). Parameters of Eqs. 12 and 13 can be found in Wolters (2014) and are thus not provided here.

The initial permeability of rock salt is representative of the permeability at WIPP.

It is noted that the crushed salt's permeability, thermal conductivity and parameter P_0 were calculated using the empirical expressions presented in Section 4.

As for the TH properties of the canister, the permeability is set to zero, the porosity to 0.01%, the thermal conductivity is 0.3 W/m °C and the specific heat is 500 J/kg °C.

5.4. Results and discussion

The results shown in this section correspond to the post-closure phase. The simulation results obtained using the C-WIPP model to describe the behavior of crushed salt are compared with the simulation results obtained using the C-WIPP/TUC model. Two values of the spacing between the waste packages along the emplacement drift are investigated: 15 m and 20 m. The decay heat in the case of a 15 m spacing is 1.3 times the decay heat shown in Fig. 5. Fig. 6 gives the locations P1, P2, P3, P4, P5 where the simulation predictions are monitored.

5.4.1. Evolution of porosity in the repository

Fig. 7 shows the evolution of porosity in the drift, near the waste package and near the roof, and in the host rock, also near the drift roof. While variations in rock salt porosity are minor (location P4), crushed salt porosity changes are considerable (locations P2 and P3), mainly due to the reconsolidation of the backfill. When using the C-WIPP model, porosity in P2 and P3 becomes nearly equal to the porosity of rock salt in less than 20 years after the backfilling of the drift (Fig. 7a), indicating a full reconsolidation of the drift. When using the C-WIPP/TUC model, the porosity in these two points after 12,000 years is 3% on average (Fig. 7b), which is approximately ten times higher than the porosity of natural salt, indicating that after 12,000 years the backfill is not yet fully compacted.

In the first year following the emplacement of the waste canister and the backfilling of the drift, the simulation using the C-WIPP/TUC model predicts an increase of porosity near the roof to 50%, approximately, due to the settling and self-compaction of the crushed salt, and thus the formation of a gap between crushed salt backfill and drift roof.

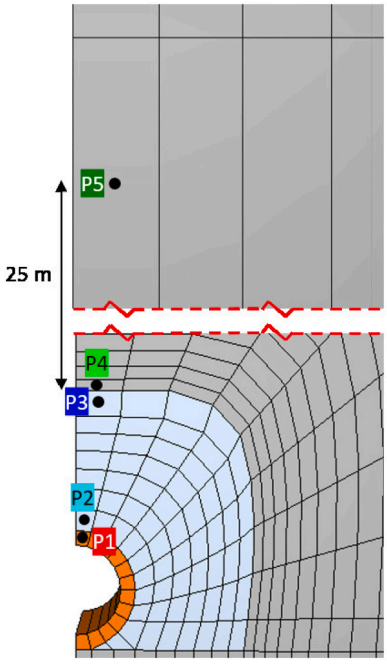

Fig. 6. Points where the simulation predictions are displayed.

Fig. 8 depicts simulated porosity maps of the drift at $t = 0$, $t = 1$ y and $t = 10$ y in the simulation using the C-WIPP/TUC model and 20 m canister spacing. At $t = 1$ y, the 2D section shows the formation of a highly porous zone in the upper elements (= gap area) and the decrease of porosity in the other grid zones. The C-WIPP model cannot accurately predict this because it does not account for the increase in porosity due to tensile stresses.

In the C-WIPP model simulation, the rate of porosity loss near the roof increases dramatically after one year (Fig. 7a). In the simulation using the C-WIPP/TUC model, the highly porous zone starts to shrink and, at 10 years, the porosity becomes less than 17% everywhere in the backfill, as shown in Fig. 8. The decrease in crushed salt porosity starting at the roof suggests a drift convergence. This convergence results from the temperature-dependent creep processes in the surrounding rock salt and is impacted by the reduction of the backfill porosity and the evolution of stress inside of it.

After 10 years, while the porosity in the backfill has already nearly reached the porosity of natural salt in the simulation using the C-WIPP model, the porosity at points P2 and P3 in Fig. 7b continues to decrease, but with a significantly slower rate. The impact of compaction-induced stress increase on the compaction rate of the crushed salt is higher in the C-WIPP/TUC model than in the C-WIPP model, in accordance with recent laboratory test results.

Moreover, reducing the spacing between the waste packages by 5 m had no significant impact on the long-term porosity evolution. However, with the C-WIPP model, porosity near the waste package started to decrease at the same time and at the same rate as near the roof, suggesting a higher creep rate of the surrounding rock salt. With the C-WIPP/TUC model, the higher creep rate also led to an earlier decrease of porosity in location P3, which becomes nearly equal to the porosity in location P2 in 5 years instead of the 10 years predicted for the 20 m spacing case.

5.4.2. Evolution of temperature in the repository

As discussed in the previous subsection, the creep of rock salt triggers the compaction of the crushed salt backfill. This creep is temperature-dependent which partly explains the changes in porosity as the spacing between the waste packages is decreased.

Fig. 9 depicts the temperature evolution near the waste package (P1 and P2), at the top of the drift (P3) and in the salt host rock (P5). Only the temperature near the waste package is affected in the short-term by the choice of the crushed salt constitutive model. The difference occurs around the first local peak observed at the waste canister (P1) and in the inner parts of the crushed salt backfill (P2) when the C-WIPP model is used. This peak is due to the low thermal conductivity of the backfill before compaction takes place, which is a result of the thermal conductivity of crushed salt being a function of porosity (Eq. 29). With the C-WIPP/TUC model, the decrease of porosity near the waste package is faster during the first few years (Fig. 7b), resulting in a higher thermal conductivity and a more progressive heat propagation around the waste package. After 10 years, despite the fact that the porosity in the C-WIPP/TUC simulations is nearly ten times higher, the thermal conductivity for a 5% porosity, using Eq. 29, is 4.8 W/m °C versus 5 W/m °C for a porosity less than 0.01, which explains why the choice of the crushed salt mechanical model is not having a significant impact on temperature results.

For the two constitutive models and spacing values, a second peak is reached in the drift area after 650 years, while the peak 25 m away in rock salt is reached after 1250 years. The temperature peaks are higher with a shorter canister spacing and so is the difference between the first and second peak in the drift area. But, most importantly, temperature rises above 100 °C, not only in the drift area but also 25 m away in the

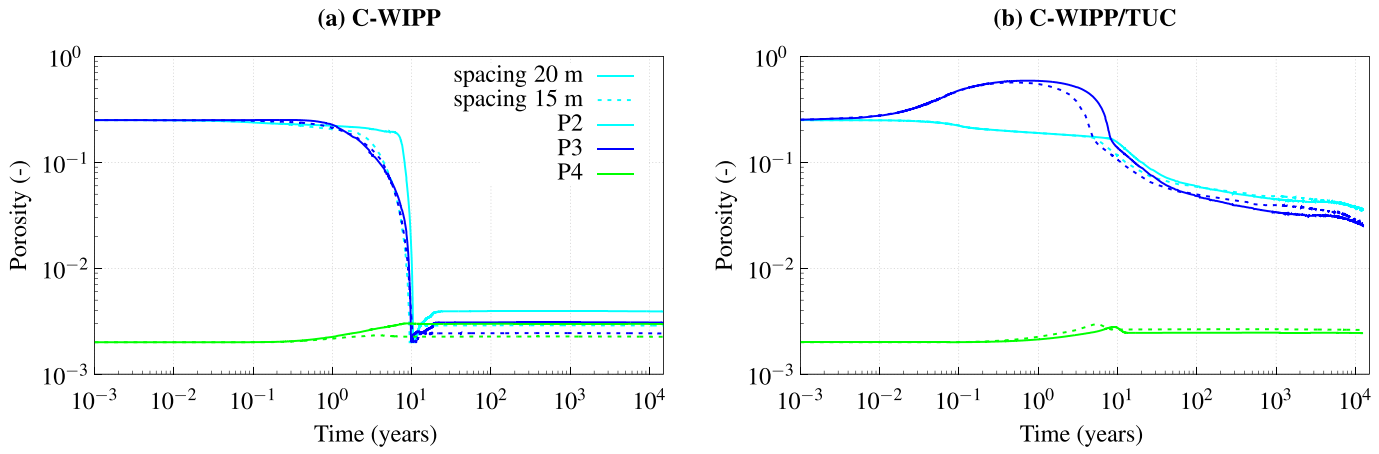

Fig. 7. Simulated porosity at three different locations for two canister spacing values, using the (a) C-WIPP model and (b) C-WIPP/TUC model.

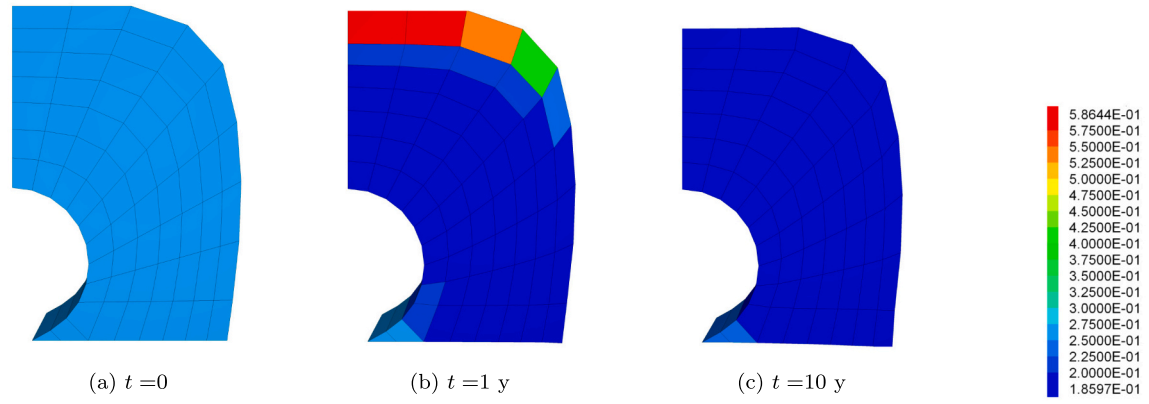

Fig. 8. Simulated 2D cross-sections of crushed salt porosity at different dates using C-WIPP/TUC model for crushed salt and a 20 m canister spacing.

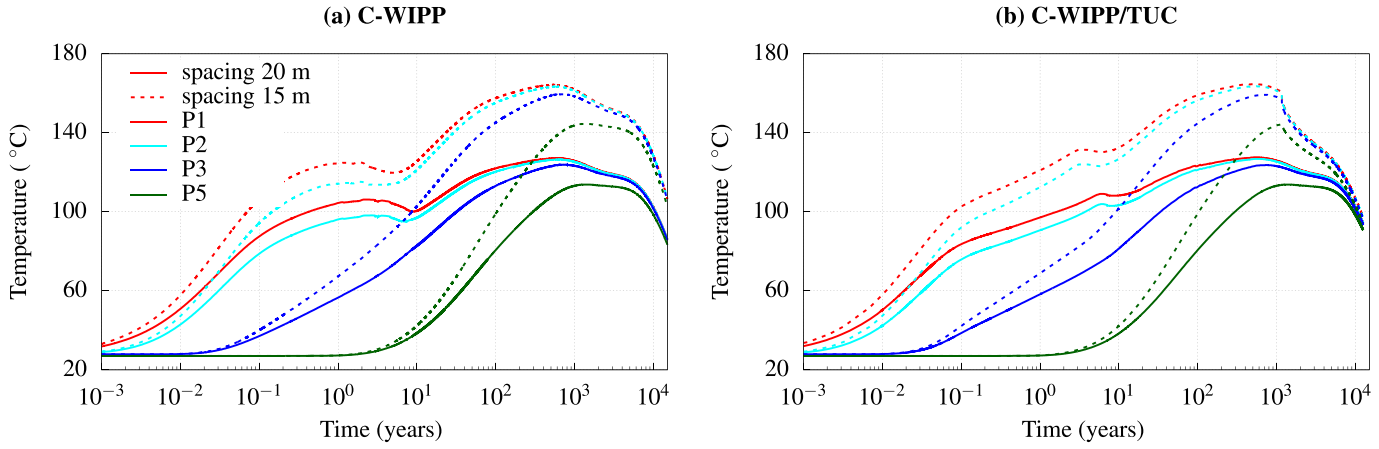

Fig. 9. Simulated temperature at four different locations for two canister spacing values, using the (a) C-WIPP model and (b) C-WIPP/TUC model.

host rock, over the course of 10,000 years, for the two spacing values.

5.4.3. Evolution of stress in the backfill

The maximum compressive total stress at locations P2 and P3 in the crushed salt backfill is shown in Fig. 10. As compaction occurs, the elastic moduli of crushed salt tend to those of intact salt, and the stress state, initially equal to zero approximately, evolves towards the initial isotropic stress state.

Because of the rapid decrease of porosity, this stress process is faster for a canister spacing of 15 m and also when employing the C-WIPP model. However, in all the conducted simulations, including the ones utilizing the C-WIPP/TUC model, where mechanical characteristics of rock salt are not yet reached in the backfill area, the initial stress state is restored in less than 50 years.

The difference between the porosity of the crushed salt backfill and the porosity of the rock salt surrounding the drift, in the simulation using the C-WIPP/TUC model, leads to a stiffness discrepancy that might be responsible for the high fluctuations in the stress results.

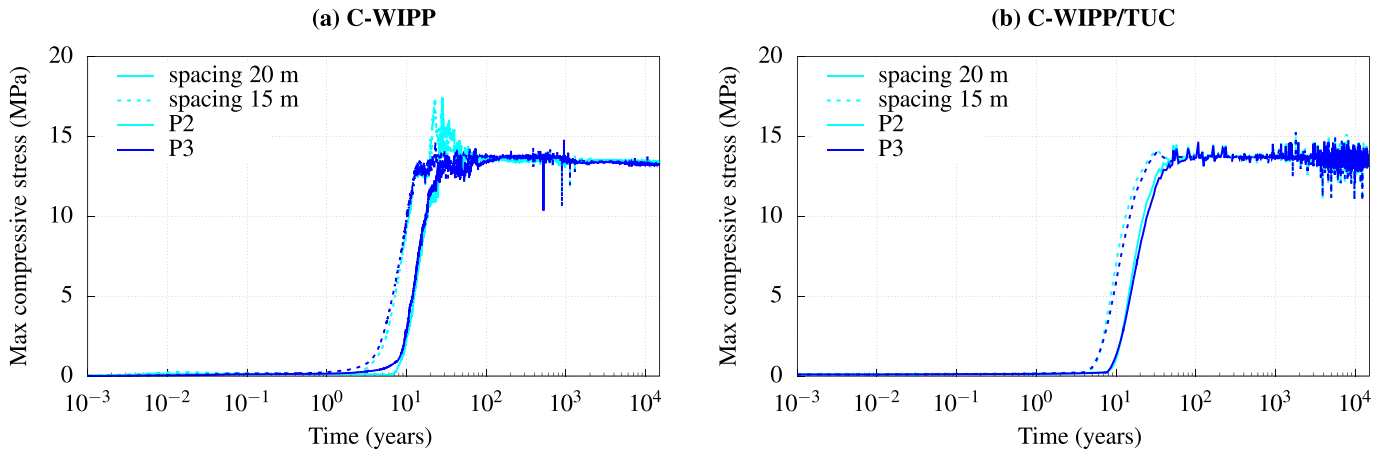

Fig. 10. Simulated maximum compressive total stress at two different locations in the backfill, for two canister spacing values, using the (a) C-WIPP model and (b) C-WIPP/TUC model.

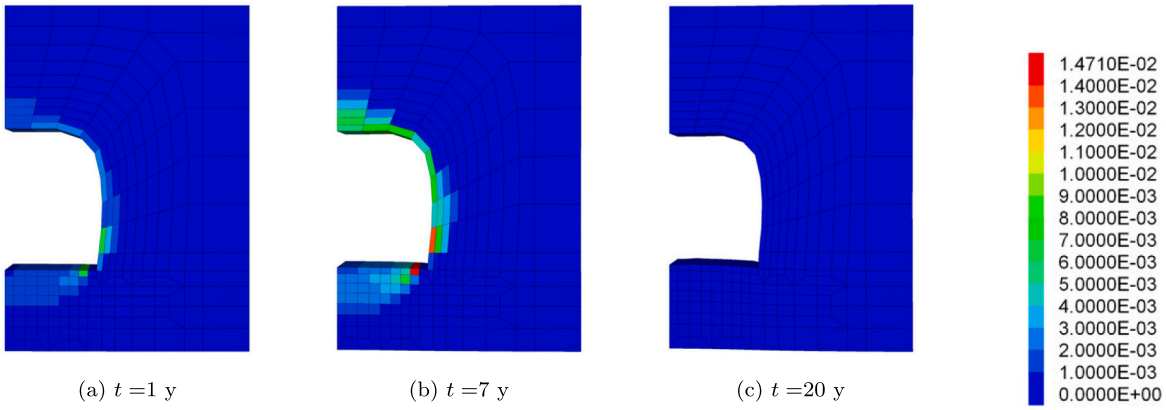

Fig. 11. Simulated dilatancy in the EDZ at different dates using the C-WIPP/TUC model and a 20 m canister spacing.

5.4.4. Evolution of the excavation damage zone

It is crucial to study the evolution of the EDZ surrounding the drift, as this is where hydraulic transport paths may form. The development and evolution of dilatancy around the drift can provide information on the EDZ's extent and evolution. As can be seen in the dilatancy maps displayed in Fig. 11, the dilatancy reaches its highest value of 1.5% at 7 years. The EDZ spans 1.1 m above and below the drift and 0.8 m around the sidewalls. At 20 years, however, rock salt around the drift becomes dilatancy-free thanks to the creep-induced healing.

When the dilatancy threshold $\varepsilon_{v,0}^{vp}$ is exceeded in the EDZ, the permeability increases significantly (Eq. 12) and reaches 10^{-17} m^2 when the dilatancy is at its maximum (see Fig. 12a). Additionally, the Biot coefficient increases up to 0.45, implying a stronger hydro-mechanical coupling in the EDZ (see Fig. 12b). At 20 years, however, their original values are restored thanks to healing.

5.4.5. Evolution of pore pressure in the repository

Figs. 13 and 14 show changes of the equivalent pore pressure (Eq. 2) and liquid saturation in the backfill (P2 and P3) and in the host rock near the drift roof (P4) and 25 m away from it (P5). The host rock is initially

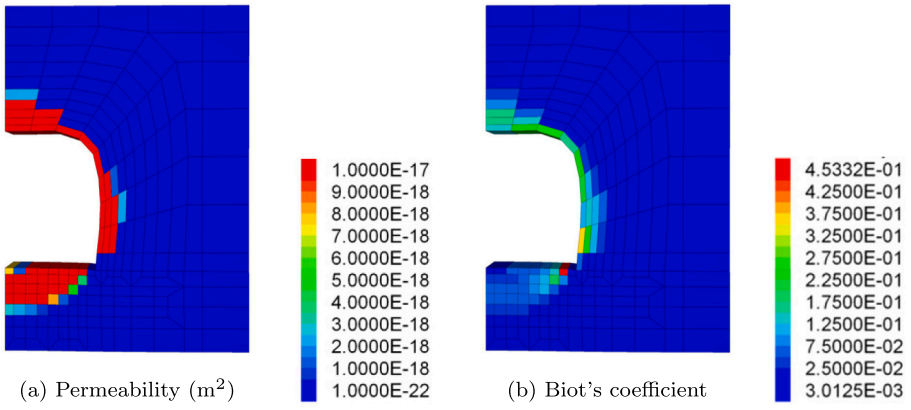

Fig. 12. Simulated permeability and Biot's coefficient in the EDZ at 7 years using the C-WIPP/TUC model and a 20 m canister spacing.

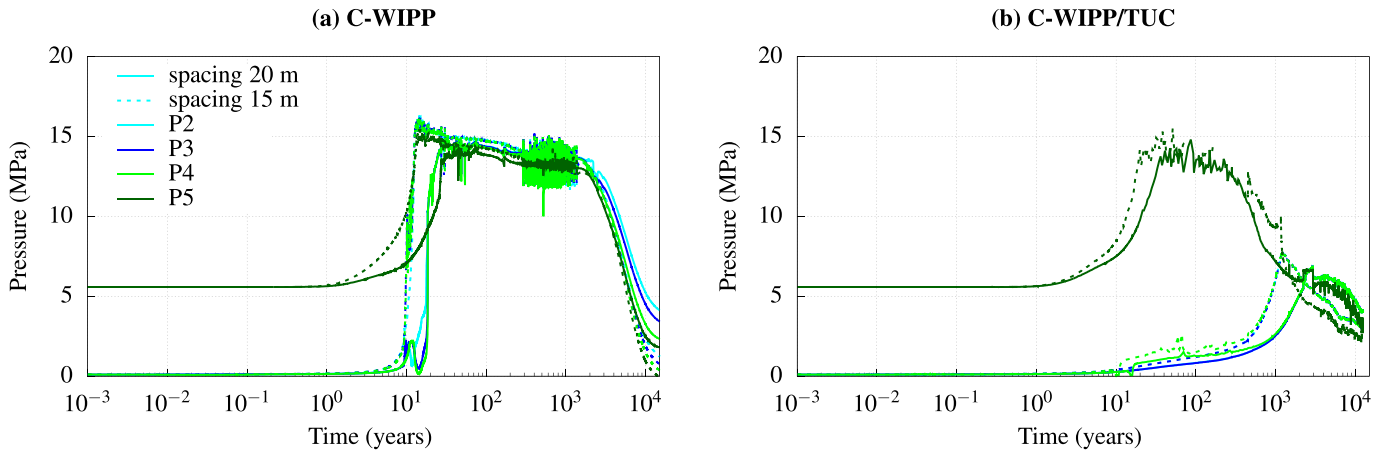

Fig. 13. Simulated equivalent pore pressure at four different locations for two canister spacing values, using the (a) C-WIPP model and (b) C-WIPP/TUC model.

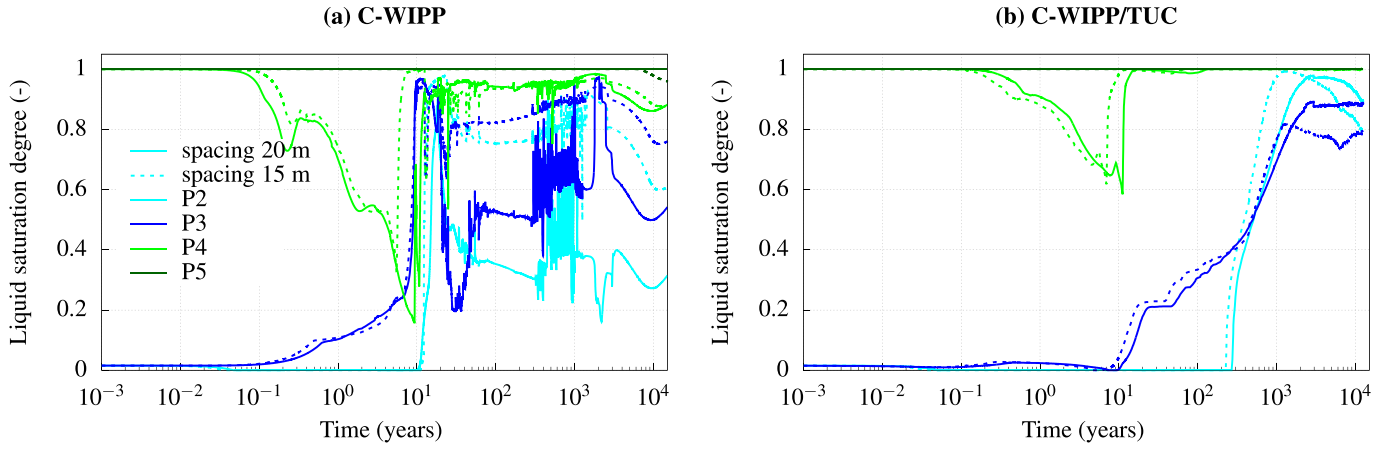

Fig. 14. Simulated liquid saturation at four different locations for two canister spacing values, using the (a) C-WIPP model and (b) C-WIPP/TUC model.

fully saturated and pore pressure is equal to the hydrostatic pressure (location P5). Near the drift, the hydrostatic pressure was modified by the drift excavation (location P4). In locations P2 and P3, pore pressure is initially set equal to the atmospheric pressure and the liquid saturation to 1.5%. In the case of a 20 m spacing, the pore pressure in location P5 starts to increase first, roughly after 2 years, while it remains constant in the other locations. Indeed, rock salt 25 m away from the drift is fully saturated and impermeable. Hence, the increase of temperature in this location at two years induces a pressurization of the pore fluid because of the discrepancy between the thermal expansion coefficients of the pore fluid and of the pore volume. The increase of pore pressure at point P4 was delayed because of the diffusion of the encapsulated air in crushed salt into the adjacent rock salt. Also, P4 being located in the EDZ, is subjected to a desaturation due to the increase of porosity and permeability before the EDZ heals.

The drift closure due to the creep of rock salt surrounding the drift triggers the reconsolidation of the backfill, resulting in an increase of crushed salt liquid saturation. With the C-WIPP model, the reconsolidation is fast. As a result, a large pore pressure develops in the four locations due to thermal pressurization; a maximum pore pressure of roughly 14 MPa is reached at 27 years in the repository for a canister spacing of 20 m. With the C-WIPP/TUC model, the maximum pore pressure of 14 MPa is reached only in P5 at 36 years. The low compaction rate of crushed salt causes a very slow increase of the liquid saturation and pore pressure near and in the backfill; a maximum pore pressure of 6.5 MPa is reached in P2, P3 and P4 at 3000 years.

With a 15 m canister spacing, the increase of pore pressure starts earlier and the maximum pore pressure value is slightly higher; 16 MPa with the C-WIPP model and 15 MPa with the C-WIPP/TUC model. In all cases, this maximum pore pressure exceeds the lithostatic stress level by roughly 1 to 2 MPa. This triggers an increase of permeability and a fluid infiltration into the salt host rock, causing an immediate decrease of pore pressure. In the simulations with the C-WIPP model, the infiltration along the grain boundaries happens in the crushed salt backfill as well, and pore pressure, in the four locations, decreases until it reaches the lithostatic stress level at 300 years and stabilizes at this level until more than 1000 years. It should be noted that the high fluctuations observed in pore pressure and saturation results in Figs. 13a and 14a are caused by the continuous changes of permeability and pore pressure due to the competition between the infiltration criterion and thermal pressurization.

In the simulations using the C-WIPP/TUC model, pore pressure in the host rock, 25 m away from the drift, does not stabilize at the lithostatic stress level but decreases at a higher rate.

As temperature decreases over time, pore pressure gradually decreases and the initial permeability of the salt formation is restored.

5.4.6. Long-term hydraulic integrity of the repository

Based on the simulation results presented in the previous subsections, it can be deduced that the choice of the crushed salt mechanical constitutive model significantly affects the model predictions of the hydraulic behavior of the repository. To illustrate this, the distribution of the logarithm of permeability in the backfill and the distribution of permeability in the salt formation at 50 years, 1000 years and 10,000

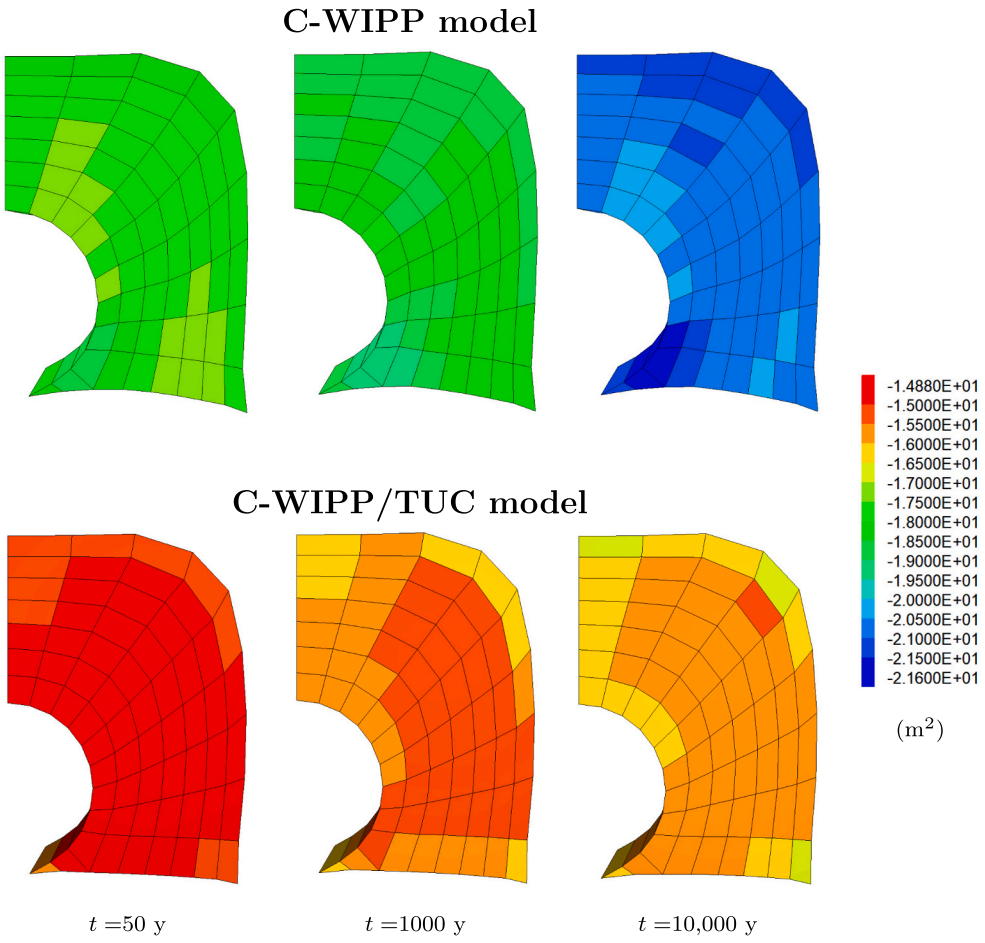

Fig. 15. Comparison of the logarithm of permeability in the backfill in the simulations using the C-WIPP and the C-WIPP/TUC model; canister spacing is 20 m.

years are displayed in Figs. 15 and 16, respectively.

With the C-WIPP model, the full reconsolidation of the backfill is quickly reached, which is highly desirable for the hydraulic integrity of the geotechnical barrier, i.e., crushed salt. However, this fast reconsolidation could trigger a significant fluid infiltration in the backfill and in the host rock that might last more than 1000 years after the emplacement of the large-sized waste packages, even when they are spaced by 20 m. According to Figs. 15 and 16, the permeability at 1000 years can go up to 10^{-18} m^2 in the backfill and up to 1.25×10^{-20} m^2 in rock salt on top of the drift. But, as temperature and thus pore pressure decrease, the hydraulic integrity and the sealing capacity of the geotechnical and the geological barriers is fully restored; permeability is less than 10^{-20} m^2 in the backfill and less than 10^{-21} m^2 in rock salt.

With the C-WIPP/TUC model, fluid infiltration is fully avoided in the backfill and is fast and far less significant in the host rock. Consequently, the permeability of rock salt would stay almost unaltered, especially in the vicinity of the drift (see permeability maps at the bottom of Fig. 16). This is not the case with the crushed salt permeability, which, due to the low compaction rate of crushed salt predicted by the C-WIPP/TUC model, would remain high, even higher than the permeability of the hydraulically-damaged crushed salt in the C-WIPP simulations. The permeability in the backfill can be as high as 2×10^{-16} m^2 after 10,000 years, indicating that the geotechnical barrier may not be completely impermeable.

6. Conclusion

This paper investigates the influence of the compaction rate of the crushed salt backfill on the short- and long-term integrity of a geological repository for nuclear waste. Using the TOUGH-FLAC simulator, coupled THM simulations of a generic salt repository are conducted. Different constitutive models are used to capture the behavior of rock salt and crushed salt. To describe the viscoplastic behavior and the time-dependent compaction of the crushed salt backfill, two viscoplastic models are compared: the C-WIPP model, which has been traditionally used in the geomechanical assessment of the integrity of the crushed salt barrier, and the new C-WIPP/TUC model, which was recently developed to enhance some of the C-WIPP model's limitations that were revealed through a systematic analysis of the plausibility of different model results as well as by recent laboratory compression experiments. In contrast to the C-WIPP model, which was calibrated using historic compaction data on specimens with a high initial porosity and then extrapolated to the range of low porosities, the C-WIPP/TUC model's parameters were calibrated over the porosity range between 16.7% and 8%.

While the C-WIPP model predicts a rapid full reconsolidation of the crushed salt backfill in less than 20 years, the C-WIPP/TUC model indicates that, after 10,000 years, the average porosity of the crushed salt backfill will be roughly 10 times that of natural salt. This difference affects the predictions of temperature, saturation degree, pore pressure, and thus the effective stress in the backfill and rock salt. Indeed, the early temperature peak that occurs within a few years of waste emplacement in the simulations using the C-WIPP model does not happen in the simulations using the C-WIPP/TUC model because the decrease of porosity in the latter is more rapid in the first year. Also, the slow reconsolidation reduces the intensity of thermal pressurization and fluid infiltration in the repository but considerably lengthens the duration that backfill stays relatively permeable (more than 10,000 years).

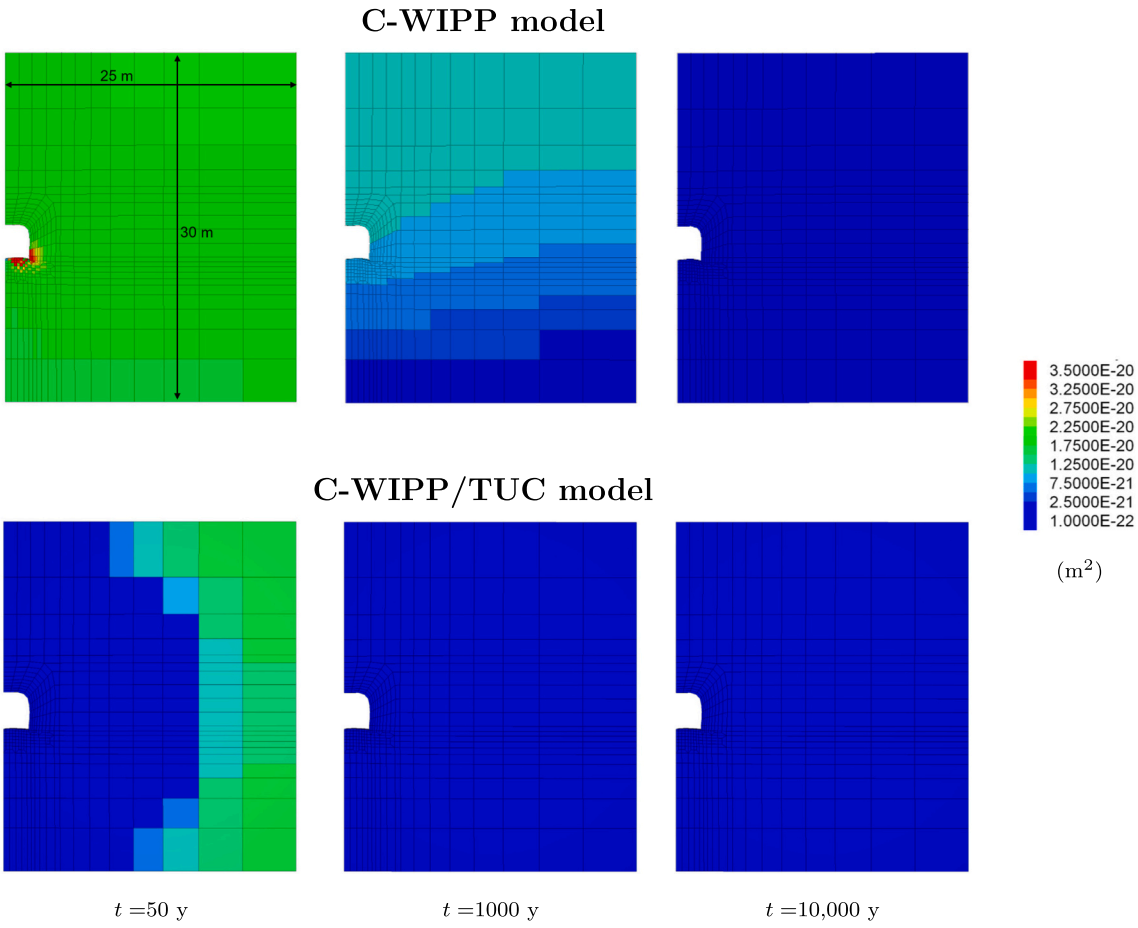

Fig. 16. Comparison of permeability in the salt host rock in the simulations using the C-WIPP and the C-WIPP/TUC model; canister spacing is 20 m.

This comparative study highlights the consequences of extrapolating beyond the range of experimental data and the importance of examining the capability of the constitutive models to capture the behavior of crushed salt in the medium and low porosity range using triaxial tests instead of uniaxial oedometer tests. However, the findings of the simulations remain preliminary, as some creep mechanisms of crushed salt, such as the compaction behavior of crushed salt at porosities below 8% have not been verified in systematic triaxial laboratory tests yet. Besides, the effect of temperature and water content on the viscous compaction of crushed salt, was not considered. In fact, it is expected that high temperatures and humidity would accelerate the compaction of crushed salt (known from systematic series of oedometric tests (Kröhn et al., 2012, 2015, 2017; Stührenberg, 2017). This is important given the high temperatures that may result from the disposal of large-sized waste packages. The effect of pore pressure on the compaction behavior of crushed salt is rarely accounted for in current granular salt constitutive models (Stormont et al., 2017) and was also disregarded in this paper. Hence, there is a need for further laboratory and field compaction data studying the effects of temperature, saturation and pore pressure. A new constitutive model, EXPO-COM, for the compaction behavior of crushed salt is currently under development at the Chair of Geomechanics and Multiphysics Systems at TUC. It incorporates the effects of different influencing factors, including temperature and water content, and is based on new lab tests from an extensive systematical lab program, which has been designed and (partially) performed with some innovative loading conditions in the framework of the joint projects KOMPASS-I and KOMPASS-II (Düsterloh et al., 2022a, 2022b). These loading conditions have been designed to isolate the individual influencing factors on the compaction behavior of crushed salt within triaxial lab tests. The investigated porosity range in these tests is between 16.7% and 2.6% instead of between 16.7% and 8%.

For the future, it is planned to refresh the investigations shown in this paper using the EXPO-COM model.

Moreover, simulations for longer time periods–more than 10,000 years–have yet to be conducted to determine when the crushed salt would approach the condition of the undisturbed host rock.

CRediT authorship contribution statement

Hafssa Tounsi: Conceptualization, Formal analysis, Investigation, Methodology, Writing – original draft, Software, Writing – review & editing. **Svetlana Lerche:** Methodology, Software, Writing – review & editing. **Ralf Wolters:** Formal analysis, Methodology, Software, Writing – review & editing. **Mengsu Hu:** Methodology, Supervision, Writing – review & editing. **Jonny Rutqvist:** Conceptualization, Funding acquisition, Methodology, Software, Supervision, Writing – review & editing, Project administration.

Declaration of Competing Interest

The authors declare that they have no known competing financial interests or personal relationships that could have appeared to influence the work reported in this paper.

Data availability

The authors do not have permission to share data.

Acknowledgements

Funding for this work has been provided by the Spent Fuel and Waste Disposition Campaign, Office of Nuclear Energy of the U.S. Department of Energy, under Contract Number DE-AC02-05CH11231 with Lawrence Berkeley National Laboratory.

This is a technical paper that does not take into account contractual limitations or obligations under the Standard Contract for Disposal of Spent Nuclear Fuel and/or High-Level Radioactive Waste (Standard Contract) (10 CFR Part 961).

To the extent discussions or recommendations in this paper conflict with the provisions of the Standard Contract, the Standard Contract governs the obligations of the parties, and this paper in no manner supersedes, overrides, or amends the Standard Contract.

This paper reflects technical work which could support future decision making by DOE. No inferences should be drawn from this paper regarding future actions by DOE, which are limited both by the terms of the Standard Contract and a lack of Congressional appropriations for the Department to fulfill its obligations under the Nuclear Waste Policy Act including licensing and construction of a spent nuclear fuel repository.

References

Bechthold, W., Smailos, E., Heusermann, S., Bollingerfehr, W., Bazargan Sabet, B., Rothfuchs, T., Kamlot, P., Grupa, J., Olivella, S., Hansen, F.D., 2004. Backfilling and Sealing of Underground Respositories for Radioactive Waste in Salt: Bambus II Project. Tech. Rep. EUR20621. European Atomic Energy Community.

Blanco-Martín, L., Rutqvist, J., Birkholzer, J.T., 2015a. Long-term modeling of the thermal–hydraulic–mechanical response of a generic salt repository for heat-generating nuclear waste. Eng. Geol. 193, 198–211. URL. https://doi.org/10.1016/j.enggeo.2015a.04.014. URL.

Blanco-Martín, L., Wolters, R., Rutqvist, J., Lux, K.-H., Birkholzer, J.T., 2015b. Comparison of two simulators to investigate thermal–hydraulic–mechanical processes related to nuclear waste isolation in saliferous formations. Comput. Geotech. 66, 219–229. URL. https://doi.org/10.1016/j.compgeo.2015b.01.021. URL.

Blanco-Martín, L., Wolters, R., Rutqvist, J., Lux, K.-H., Birkholzer, J.T., 2016. Thermal–hydraulic–mechanical modeling of a large-scale heater test to investigate rock salt and crushed salt behavior under repository conditions for heat-generating nuclear waste. Comput. Geotech. 77, 120–133. https://doi.org/10.1016/j.compgeo.2016.04.008.

Blanco-Martín, L., Rutqvist, J., Birkholzer, J.T., 2017. Extension of TOUGH-FLAC to the finite strain framework. Comput. Geosci. 108, 64–71. https://doi.org/10.1016/j.cageo.2016.10.015.

Callahan, G., Mellegard, K., Hansen, F., 1998. Constitutive Behavior of Reconsolidating Crushed Salt. Tech. Rep. SAND-98-0179C. Sandia National Laboratories, Albuquerque, NM (USA).

Camphouse, R., Gross, M., Herrick, C., Kicker, D., Thompson, B., 2012. Recommendations and Justifications of Parameter Values for the Run-of-Mine Salt Panel Closure System Design Modeled in the PCS-2012 PA. Tech. Rep. Memo 5412. Sandia National Lab.(SNL-NM), Albuquerque, NM (United States).

Carter, J., Hansen, F., Kehrman, R., Hayes, T., 2011. A Generic Salt Repository for Disposal of Waste from a Spent Nuclear Fuel Recycle Facility. Tech. Rep. SRNL-RP-2011-00149. Savannah River National Laboratory.

Chen, J., Ren, S., Yang, C., Jiang, D., Li, L., 2013. Self-healing characteristics of damaged rock salt under different healing conditions. Materials 6 (8), 3438–3450. https://doi.org/10.3390/ma6083438.

Cosenza, P., Ghoreychi, M., Bazargan-Sabet, B., De Marsily, G., 1999. In situ rock salt permeability measurement for long term safety assessment of storage. Int. J. Rock Mech. Min. Sci. 36 (4), 509–526. https://doi.org/10.1016/S0148-9062(99)00017-0.

Coussy, O., 2004. Poromechanics. John Wiley & Sons.

Czaikowski, O., Friedenberg, L., Wieczorek, K., Müller-Hoeppe, N., Lerch, C., Eickemeier, R., Laurich, B., Liu, W., Strührenberg, D., Svensson, K., Zemke, K., Lüdeling, C., Popp, T., Bean, J., Mills, M., Reedlunn, B., Düsterloh, U., Lerche, S., Zhao, J., 2020. KOMPASS: Compaction of Crushed Salt for the Safe Containment. Tech. Rep. SAND-2020-11692R; GRS-608692225. Sandia National Lab.(SNL-NM), Albuquerque, NM (United States).

DBE, 2001. Numerische Untersuchungen zum Konvergenzverhalten eines Einzelhohlraumes. Tech. Rep. 22341011. DBE Technology GmbH, Peine, Germany.

Düsterloh, U., Lerche, S., Saruulbayar, N., 2022a. Crushed salt compaction-a new approach for lab test analysis, physical modeling and numerical simulation: Part 2: Numerical application. In: The Mechanical Behavior of Salt X. CRC Press, pp. 314–327.

Düsterloh, U., Lerche, S., Saruulbayar, N., 2022b. Crushed salt compaction-a new approach for lab test analysis, physical modelling and numerical simulation: Part 1: Development and validation. In: The Mechanical Behavior of Salt X. CRC Press, pp. 301–313.

Hansen, F.D., Leigh, C.D., 2011. Salt Disposal of Heat-Generating Nuclear Waste. Tech. Rep. SAND2011-0161. Sandia National Laboratories, Albuquerque, NM (USA). https://doi.org/10.2172/1005078. URL.

Hou, Z., 2002. Geomechanische Planungskonzepte für untertägige Tragwerke mit besonderer Berücksichtigung von Gefügeschädigung. Verheilung und hydromechanischer Kopplung, Papierflieger, Clausthal-Zellerfeld, Germany.

Hu, M., Steefel, C.I., Rutqvist, J., 2021. Microscale mechanical-chemical modeling of granular salt: Insights for creep. J. Geophys. Res. Solid Earth 126 (12), e2021JB023112. URL. https://doi.org/10.1029/2021JB023112. URL.

Hunsche, U., Hampel, A., 1999. Rock salt—the mechanical properties of the host rock material for a radioactive waste repository. Eng. Geol. 52 (3–4), 271–291. URL. https://doi.org/10.1016/S0013-7952(99)00011-3. URL.

Itasca FLAC3D, 2012. 5.0 (Fast Lagrangian Analysis of Continua in 3 Dimensions) Manual [55401].

Kansy, A., 2007. Einfluss des Biot-Parameters auf das hydraulische Verhalten von Steinsalz unter der Berücksichtigung des Porendruckes. Ph.D. thesis. Technische Universität Clausthal, Clausthal-Zellerfeld, Germany.

Kim, J., Tchelepi, H.A., Juanes, R., 2011. Stability and convergence of sequential methods for coupled flow and geomechanics: Fixed-stress and fixed-strain splits. Comput. Methods Appl. Mech. Eng. 200 (13–16), 1591–1606. URL. https://doi.org/10.1016/j.cma.2010.12.022. URL.

Kim, J., Sonnenthal, E.L., Rutqvist, J., 2012. Formulation and sequential numerical algorithms of coupled fluid/heat flow and geomechanics for multiple porosity materials. Int. J. Numer. Methods Eng. 92 (5), 425–456. https://doi.org/10.1002/nme.4340.

Kröhn, K., Zhang, C., Wolf, J., Stührenberg, D., Jobmann, M., von Borstel, L., Lerch, C., 2012. The compaction behaviour of salt backfill at low porosities. In: Proceedings of the 7th International. Conference on the Mechanical Behavior of Salt (SaltMech7), Paris, France, pp. 155–162.

Kröhn, K.-P., Zhang, C.-L., Czaikowski, O., Stührenberg, D., Heemann, U., 2015. The compaction behaviour of salt backfill as a THM-process. In: Proceedings of 8th Conference on Mechanical Behavior Salt (SaltMech8), pp. 49–59.

Kröhn, K.-P., Stührenberg, D., Jobmann, M., Heemann, U., Czaikowski, O., Wieczorek, K., Müller, C., Zhang, C.-L., Moog, H., Schirmer, S., Friedenberg, L., 2017. Mechanical and hydraulic behaviour of compacting crushed salt backfill at low porosities. Project repoperm. Phase 2. Tech. Rep. GRS-450. Gesellschaft für Anlagen-und Reaktorsicherheit (GRS) gGmbH.

Kuhlman, K.L., Sevougian, S.D., 2013. Establishing the Technical Basis for Disposal of Heat-Generating Waste in Salt. Tech. Rep. SAND2013-6212P. Sandia National Laboratories, Albuquerque, NM (USA).

Lerch, C., Bollingerfehr, W., Filbert, W., Zhang, Q., 2012. Thermo-mechanical analyses for evaluating a HLW-repository concept. In: Proceedings of the 7th International. Conference on the Mechanical Behavior of Salt (SaltMech7), Paris, France, pp. 433–442.

Lerche, S., 2012. Kriech-und Schädigungsprozesse im Salinargebirge bei mono-und multizyklischer Belastung. Ph.D. thesis. Technische Universität Clausthal, Clausthal-Zellerfeld, Germany.

Leverett, M., 1941. Capillary behavior in porous solids. Trans. AIME 142 (01), 152–169.

Lux, K., Lerche, S., Dyogtyev, O., 2018. Intense damage processes in salt rock-a new approach for laboratory investigations, physical modelling and numerical simulation. In: Mechanical Behavior of Salt IX, Hannover, Germany, pp. 12–14.

Mönig, J., Beuth, T., Wolf, J., Lommerzheim, A., Mrugalla, S., 2013. Preliminary safety analysis of the gorleben site: Safety concept and application to scenario development based on a site-specific features, events and processes (FEP) database–13304. In: WM2013 Conference, Phoenix, AZ, USA.

Olivella, S., Gens, A., 2002. A constitutive model for crushed salt. Int. J. Numer. Anal. Methods Geomech. 26 (7), 719–746. https://doi.org/10.1002/nag.220.

Olivella, S., Castagna, S., Alonso, E., Lloret, A., 2011. Porosity variations in saline media induced by temperature gradients: experimental evidences and modelling. Transp. Porous Media 90 (3), 763–777. URL. https://doi.org/10.1007/s11242-011-9814-x. URL.

Pruess, K., Oldenburg, C., Moridis, G., 2012. TOUGH2 User's Guide, Version 2.0 report lbnl-43134.

Rutqvist, J., 2020. Thermal management associated with geologic disposal of large spent nuclear fuel canisters in tunnels with thermally engineered backfill. Tunn. Undergr. Space Technol. 102, 103454. URL. https://doi.org/10.1016/j.tust.2020.103454. URL.

Rutqvist, J., Wu, Y.-S., Tsang, C.-F., Bodvarsson, G., 2002. A modeling approach for analysis of coupled multiphase fluid flow, heat transfer, and deformation in fractured porous rock. Int. J. Rock Mech. Min. Sci. 39 (4), 429–442. https://doi.org/10.1016/S1365-1609(02)00022-9.

Sjaardema, G., Krieg, R.D., 1987. A Constitutive Model for the Consolidation of WIPP Crushed Salt and its Use in Analyses of Backfilled Shaft and Drift Configurations. Tech. Rep. SAND-87-1977. Sandia National Laboratories, Albuquerque, NM (USA).

Spiers, C., Schutjens, P., Brzesowsky, R., Peach, C., Liezenberg, J., Zwart, H., 1990. Experimental determination of constitutive parameters governing creep of rocksalt by pressure solution. Geol. Soc. Lond., Spec. Publ. 54 (1), 215–227. URL. https://doi.org/10.1144/GSL.SP.1990.054.01.2. URL.

Stormont, J., Lampe, B., Mills, M., Paneru, L., Lynn, T., Piya, A., 2017. Improving the Understanding of the Coupled Thermal-Mechanical-Hydrologic Behavior of Consolidating Granular Salt. Tech. Rep. NEUP project 13–4834. Univ. of New Mexico, Albuquerque, NM (United States).

Stührenberg, D., 2017. Long-term laboratory investigation on backfill. In: The Mechanical Behavior of Salt–Understanding of THMC Processes in Salt. CRC Press, pp. 223–229.

Sweet, J., McCreight, J., 1983. Thermal conductivity of rocksalt and other geologic materials from the site of the proposed waste isolation pilot plant. In: Thermal Conductivity 16. Springer, pp. 61–78.

Tounsi, H., Rutqvist, J., Hu, M., Wolters, R., Lerche, S., 2023. Long-term sinking of nuclear waste canisters in salt formations by low-stress creep at high temperature. Acta Geotech. 1–16. URL. https://doi.org/10.1007/s11440-023-01900-w. URL.

Urai, J., Spiers, C., 2017. The effect of grain boundary water on deformation mechanisms and rheology of rocksalt during long-term deformation. In: The Mechanical Behavior of Salt–Understanding of THMC Processes in Salt. CRC Press, pp. 149–158.

Winterle, J., Ofoegbu, G., Pabalan, R., Manepally, C., Mintz, T., Pearcy, E., Fedors, R., 2012. Geologic Disposal of High-Level Radioactive Waste in Salt Formations. Tech. Rep. NRC-02-07-006. US Nuclear Regulatory Commission.

Wolters, R., 2014. Thermisch-hydraulisch-mechanisch gekoppelte Analysen zum Tragverhalten von Kavernen im Salinargebirge vor dem Hintergrund der Energieträgerspeicherung und der Abfallentsorgung: ein Beitrag zur Analyse von Gefügeschädigungsprozessen und Abdichtungsfunktion des Salinargebirges im Umfeld untertätiger Hohlräume. Ph.D. thesis,. Technische Universität Clausthal, Clausthal-Zellerfeld, Germany.

Wolters, R., Lux, K.-H., Düsterloh, U., 2012. Evaluation of rock salt barriers with respect to tightness: Influence of thermomechanical damage, fluid infiltration and sealing/healing. In: Mechanical Behaviour of Salt VII. CRC Press, pp. 439–448.